



AMERICAN METEOROLOGICAL SOCIETY

Journal of Climate

EARLY ONLINE RELEASE

This is a preliminary PDF of the author-produced manuscript that has been peer-reviewed and accepted for publication. Since it is being posted so soon after acceptance, it has not yet been copyedited, formatted, or processed by AMS Publications. This preliminary version of the manuscript may be downloaded, distributed, and cited, but please be aware that there will be visual differences and possibly some content differences between this version and the final published version.

The DOI for this manuscript is doi: 10.1175/JCLI-D-17-0642.1

The final published version of this manuscript will replace the preliminary version at the above DOI once it is available.

If you would like to cite this EOR in a separate work, please use the following full citation:

Liu, C., and R. Allan, 2018: Unrealistic increases in wind speed explain reduced eastern Pacific heat flux in reanalyses. *J. Climate*. doi:10.1175/JCLI-D-17-0642.1, in press.

© 2018 American Meteorological Society



1
2
3
4
5
6
7
8
9
10
11
12
13
14
15
16
17
18
19

Unrealistic increases in wind speed explain reduced eastern Pacific heat flux in reanalyses

Chunlei Liu^{1,2} and Richard P. Allan^{1,2,3}

¹ *Department of Meteorology, University of Reading, Reading, UK,*

² *National Centre for Earth Observation, Reading, UK,*

³ *National Centre for Atmospheric Science, Reading, UK*

Corresponding author address: Chunlei Liu, Department of Meteorology, University of Reading,

Reading, UK, RG6 6BB

E-mail: c.l.liu@reading.ac.uk

ABSTRACT

Tropical eastern Pacific sea surface temperature plays a pivotal role in mechanisms that determine global mean surface temperature variability. In this study, the surface flux contribution to recent cooling of the tropical eastern Pacific is investigated using data from three atmospheric reanalyses with full assimilation of observations, an observations-based net surface energy flux reconstruction and fifteen atmospheric-only climate model simulations. For the ERA-Interim reanalysis, 78% of the decrease in net surface flux ($-0.65 \text{ Wm}^{-2}\text{yr}^{-1}$ over 1988-2008) is explained by the latent heat flux variability. Latent heat flux variability differs between datasets and this is investigated using a bulk formula. We find that discrepancies in wind speed change explain contrasting latent heat flux trends across datasets. The significant increase of $0.26 \text{ ms}^{-1}\text{decade}^{-1}$ in wind speed over the tropical eastern Pacific in the ERA-Interim reanalysis is not reproduced by satellite or buoy observations and atmospheric-only climate model simulations, casting questions on the reliability of reanalysis-based surface fluxes over the tropical eastern Pacific.

Key points:

- 1) Latent heat flux explains decreasing surface heat flux trend over tropical eastern Pacific area.
- 2) Near surface wind speed change is the main driver of the latent heat flux variability.
- 3) Changes in heat flux over the tropical eastern Pacific depicted by reanalyses estimates are unrealistic

Key words: Global warming slowdown, tropical eastern Pacific cooling, Surface flux contribution, Reliability

41 **1. Introduction**

42 Cooling over the Tropical Eastern Pacific (*TEP*) has been identified as an important factor in
43 explaining the mechanisms leading to suppressed global warming at the beginning of the 21st century
44 [*Easterling and Werner, 2009; Knight et al., 2009; Trenberth and Fasullo, 2013; Huber and Knutti,*
45 *2014; Watanabe et al., 2014; Kosaka and Xie, 2013; Meehl et al., 2014; England et al., 2015*]. Using
46 both NOAA (National Oceanic and Atmospheric Administration) 20th century [*Compo et al., 2011*]
47 and ECMWF (European Centre for Medium-Range Weather Forecasts) Interim Reanalysis (ERA-
48 Interim) [*Dee et al., 2011*] atmospheric reanalysis data, as well as model simulations, *England et al.*
49 [*2014*] found that the cooling is due to the observed pronounced strengthening in Pacific trade winds
50 which enhance the ocean heat uptake and the upwelling of the subsurface cold water over the *TEP*
51 area. *Zhou et al.* [*2016*] found that the sea surface temperature (*SST*) pattern-induced low cloud
52 increase [*Norris and Evan, 2015*] over the *TEP* region can enhance the shortwave reflection and
53 modify the Earth's energy budget. This has been linked to changes in atmospheric stability and can
54 explain increases in climate sensitivity relating to the evolution of *SST* patterns in response to
55 radiative forcing [*Ceppi and Gregory, 2017; Andrews and Webb, 2017*]. The cloud feedback on *SST*
56 changes over the decadal time scale can amplify cooling in *TEP* region where air descends. *Brown et*
57 *al.* [*2014*] also showed that cooling may be enhanced in both duration and magnitude by increasing
58 the shortwave reflection (*RSW*) over *TEP* region, where the reduced outgoing longwave radiation
59 (*OLR*) cannot fully compensate the shortwave reflection, due to the relatively cool marine stratiform
60 clouds present [*Klein and Hartmann, 1993*], reducing the net downward surface energy flux (F_s) and
61 cooling the surface.

62

63 On one hand, the cooling *TEP* will suppress the longwave radiation and the turbulent energy
64 transfer from ocean to the atmosphere, so the net downward energy flux will be increased over this
65 region, as depicted by the AMIP (Atmospheric Model Intercomparison Project) model simulations

66 [Liu et al., 2015]. On the other hand, increased winds [England et al., 2014] will cause more
67 evaporation, so more latent heat may be lost to the atmosphere and decrease the net downward
68 energy flux. In order to further understand the mechanisms and driving factors of the *TEP* cooling,
69 different surface flux data from atmospheric reanalyses, observational reconstructions [Liu et al.,
70 2017] and AMIP5 simulations are used to study the surface energy flux contributions to the *TEP*
71 cooling in this study. Considering the imperfect temporal homogeneities in parameterized reanalysis
72 fluxes [Berrisford et al. 2011; Balmaseda et al. 2013; von Schuckmann et al., 2016], the detailed
73 analysis of the reasons causing the spurious changes is conducted in this study using a bulk formula,
74 so as to investigate the role of meteorological variables in determining latent heat flux changes.

75

76 **2. Data and method**

77 The three atmospheric reanalyses used in this study are ECMWF ERA-Interim reanalysis [Dee et
78 al., 2011; Berrisford et al., 2011] (hereinafter referred to as ERA-Interim). JRA55 (the Japanese 55-year
79 Reanalysis, [Kobayashi et al. 2015]) and MERRA2 (Modern Era-Retrospective Analysis for
80 Research and Applications, [Gelaro et al., 2017]). Surface fluxes, including the surface shortwave
81 (*SW*) and longwave (*LW*) radiation fluxes, the latent heat (*LH*) and sensible heat (*SH*) turbulent
82 fluxes, forecasted directly by the reanalyses, are used. The monthly fluxes available for this study are
83 averaged from the forecast every 12 hours for ERA-Interim, every 6 hours for JRA55 and every hour for
84 MERRA2. A four-dimensional variational analysis is used in ERA-Interim and JRA55 reanalyses,
85 and a three-dimensional variational data assimilation in MERRA2, where data from the full
86 observing system are assimilated. The derived net surface heat fluxes based on the atmospheric
87 energy tendencies and transports of ERA-Interim and TOA (top of atmosphere) satellite radiation budget
88 data [Allan et al., 2014; Liu et al., 2015, 2017] are also exploited based on results from the DEEPC
89 (Diagnosing Earth's Energy Pathways in the Climate system) project. DEEPC takes advantages of
90 the assimilation of full observations in ERA-Interim and the observed energy budget of the Earth

91 system [Liu et al., 2015], the atmospheric energy transports are mass corrected [Trenberth et al.
92 1995; Chiodo and Haimberger, 2010; Mayer and Haimberger, 2012] and the land surface fluxes are
93 adjusted based on the energy budget conservation [Liu et al., 2017] and has applications in a number
94 of previous studies [Williams et al., 2015; Valdivieso et al., 2015; Senior et al., 2016; Roberts et al.,
95 2017]. The CERES (Clouds and the Earth’s Radiant Energy System [Loeb et al., 2012]) surface
96 radiation fluxes are used to infer the surface turbulent fluxes from DEEPC net surface flux.

97

98 The bulk formula used to calculate the latent heat fluxes at surface is from Singh et al. [2005],

$$99 \quad LH = \rho L C_E U (Q_s - Q_a) \quad (1)$$

100 where ρ is the air density, L is the latent heat of evaporation, C_E is bulk transfer coefficient for water
101 vapor (also called the Dalton number) and can be estimated using near surface wind speed (Bentamy
102 et al. 2003), U is the wind speed at a height of typically 10 m, Q_s is the saturation specific humidity
103 at the surface and can be estimated using *SST* and sea level pressure, and Q_a is the near-surface
104 specific humidity at the atmospheric measurement level and can be empirically estimated from *SST*
105 and the total column water vapor content (please see Singh et al. [2005] for the detailed
106 descriptions). The *LH* estimation is specially designed to use satellite observations. The four input
107 fields are the total column water vapour content (*WV*), near surface wind speed, *SST* and mean sea
108 level pressure (*MSLP*), which are all available as analysis time variables from the reanalyses.
109 Considering the good temporal homogeneity of the SSM/I data (Fig. S1), the observed *WV* and *U*
110 from SSM/I are employed and the time series is constructed using F08, F11 and F13 datasets. The
111 wind speed has a general increasing trend before 2009, but decreases after 2012 (Fig. S1a). The data
112 from 15 AMIP5 model simulations are also used, with prescribed observed *SST* and sea ice and
113 realistic radiation forcings [Taylor et al., 2012]. The wind speed data from TAO (Tropical
114 Atmosphere Ocean) moored buoy array [TAO Project Office, 2000] are also used for comparison. All
115 datasets are listed in Table 1 with some brief descriptions.

116

117 3. Results

118 3.1 Trends in surface heat flux

119 The net surface heat flux trends from ERAINT, DEEPC and AMIP5 ensemble mean over 1988-
120 2008 are shown in Fig. 1, together with the ERAINT *SST* trend. The corresponding area mean
121 anomaly time series over *TEP* are also plotted on the right column. The trends of ERAINT *SST*
122 ($-0.06 \text{ K decade}^{-1}$) and net surface flux from DEEPC ($-0.32 \text{ Wm}^{-2}\text{yr}^{-1}$) and ERAINT ($-0.65 \text{ Wm}^{-2}\text{yr}^{-1}$)
123 show a consistent negative trend over *TEP* (Figs. 1a-c). The DEEPC F_s is based on a combination of
124 satellite data and ERAINT atmospheric energy transports but does not use the simulated surface
125 fluxes. While both datasets display a negative trend in downward net heat flux over *TEP*, the DEEPC
126 trend is smaller in magnitude than that of ERAINT (Figs. 1f and g). The strong negative trend can
127 also be seen from JRA55 data (Fig. S2a), but is weak in MERRA2 data (Fig. S2b) and not present in
128 AMIP5 ensemble mean simulations (Fig. 1d). Both trends from ERAINT and JRA55 (Fig. 1c and
129 Fig. S2a) show similar spatial patterns, with negative trends over central Indian Ocean, western and
130 eastern Pacific, but positive trends in northeastern Pacific. A contrasting pattern is produced by
131 MERRA2: the trend over northeastern Pacific is negative but positive over most of the *TEP* area.
132 Trend patterns in *SST* (Fig. 1a) and AMIP5 ensemble mean simulated F_s (Fig.1d) are anti-correlated,
133 indicating that reducing *SST* leads to reduced heat loss to the atmosphere so more surface flux into
134 the ocean (increased F_s). While in contrast this is not seen in DEEPC (Fig. 1b) and ERAINT (Fig.
135 1c). Although the input data used to generate the DEEPC product are not fully coupled, it is
136 considered the best representation of the coupled system available to us. The errors can be introduced
137 from incomplete coverage, biases and model inadequacies during observational input to ERAINT,
138 but it is representative of the coupled system, in which heat fluxes can drive changes in *SST* (e.g.
139 reduced F_s can cool the ocean and reduce *SST*).

140

141 The deseasonalized anomaly time series of F_s and its four components (SW , LW , SH and LH) over
142 TEP are plotted in Figs. 1g-h and Figs. S2c-d; the reference period for the anomaly calculation is
143 from 2001-2008. It is clear that the LH variation dominates the F_s variability in three atmospheric
144 reanalyses and the AMIP5 ensemble mean. The LH trend follows the corresponding F_s trend and the
145 correlation coefficients (r) between LH and F_s over 1988-2008 are 0.97, 0.94, 0.90 and 0.96, the LH
146 trend magnitudes are 78%, 98%, 169% and 44% of the F_s trends for ERAINT, JRA55, MERRA2 and
147 the AMIP5 ensemble mean, respectively. The turbulent fluxes (SH and LH) are also derived from
148 the difference of the DEEPC net surface energy fluxes and the CERES surface radiation fluxes and
149 the anomaly time series is plotted in Fig. 1f. The corresponding correlation coefficient between
150 turbulent flux and F_s over 2002-2015 is 0.98. It is apparent that SW and F_s variability are also well
151 correlated ($r = 0.69, 0.72, 0.73$ and 0.56 for ERAINT, JRA55, MERRA2 and AMIP5 ensemble
152 mean, respectively), but the SW trend is generally smaller than the F_s trend. The corresponding SW
153 trend contribution to the F_s trend is 22% for ERAINT and 11% for JRA55, and the contribution of
154 31% in AMIP5 ensemble mean is relatively strong. The SW trend in MERRA2 is in opposite sign
155 with F_s trend. All these correlation coefficients are significant based on the two-tailed test using
156 Pearson critical values at the level of 5% and the trends (except for the LH trend of AMIP5) are also
157 significant using Mann-Kendall test at a significance level of 0.05 [Hipel and McLeod, 1994], which
158 emphasise that the evaporation dominates variabilities and trends in surface fluxes in the equatorial
159 eastern Pacific.

160

161 Both ERAINT and JRA55 show strong downward F_s trends of $0.65 \text{ Wm}^{-2}\text{yr}^{-1}$ and $0.50 \text{ Wm}^{-2}\text{yr}^{-1}$
162 over 1988-2008, respectively. MERRA2 also shows a weak negative trend in F_s ($-0.13 \text{ Wm}^{-2}\text{yr}^{-1}$) and
163 LH ($-0.22 \text{ Wm}^{-2}\text{yr}^{-1}$). Considering the global changes may include spurious jumps, as a very crude
164 adjustment, the global mean F_s trend over the same period shown in Fig. S2e is removed, and the
165 corresponding F_s trends over TEP are $-0.53, -0.29$ and $-0.35 \text{ Wm}^{-2}\text{yr}^{-1}$ for ERAINT, JRA55 and

166 DEEPC, respectively. They are all significant using Mann-Kendall test at a significance level of
167 0.05. Considering the ocean heat capacity of $4.2 \times 10^6 \text{ J/K/m}^2/\text{m}$, the mean mixing depth of 100m over
168 eastern Pacific [Roberts *et al.*, 2017] and F_s is 3 Wm^{-2} lower in the 2000s vs the 1990s, the estimated
169 temperature change $\Delta T \approx -2.3 \text{ K}$ is too large considering the observed ocean temperature change over
170 *TEP* area (Fig. 1e). This suggests that either the trends are unrealistic or changes in ocean heat
171 transport convergence offset these surface heat flux changes. It is noticed that there are
172 discontinuities in global area mean F_s time series of MERRA2 (Fig. S2e): it has a step change near
173 1992, a large negative trend between 1992 and 2008 and an anomalous positive trend after 2009.
174 Since the DEEPC global mean net surface flux is well constrained by the TOA satellite observations
175 [Allan *et al.*, 2014] and the zero global atmospheric energy convergence [Liu *et al.*, 2015, 2017], so
176 the global mean F_s from DEEPC product can be regarded as realistic, and any large trend deviation
177 in the global mean time series from that of DEEPC data can be questioned. It is also noticed both F_s
178 and LH trends from MERRA2 over *TEP* differ with the other two atmospheric reanalyses.

179 The contributions of SW fluxes to the net surface flux trends over *TEP* are significant for the later
180 periods ($-0.50 \text{ Wm}^{-2}\text{yr}^{-1}$ for 1995-2015 in ERAINT and $-0.42 \text{ Wm}^{-2}\text{yr}^{-1}$ over 2000-2015 for JRA55),
181 consistent with evidence of increased low cloud cover (*LCC*) [Norris and Evan, 2015; Zhou *et al.*,
182 2016]. However, for the longer 1988-2008 period, LH is found to dominate the changes in F_s .

183

184

185 **3.2 Sensitivity of latent heat flux to atmospheric variables**

186 Since the LH change dominates the F_s variability over *TEP* in three atmospheric reanalyses,
187 observation and AMIP5 simulation ensemble mean, it is necessary to investigate the driver for the
188 LH change. In order to do this, the bulk formula developed by Singh *et al.* [2005] is employed to
189 compute LH . This bulk formula is designed for the application of satellite observations so only four
190 meteorological variables are required for input: *SST*, *MSLP*, *WV* and *U* (near surface wind speed,

191 generally at 10m). For the sensitivity test, climatologies of four fields are applied, and each time-
192 varying individual field is subsequently substituted into the bulk formula to isolate the contribution
193 of the determinant variables. Effects on *LH* trend from the different *SST* and *MSLP* datasets are
194 similar, so are not shown and discussed here. An unrealistic decline in global area mean ERAINT
195 *WV* around 1991-1993 compared with SSM/I observations [Allan *et al.* 2014; Allan, 2017] was
196 removed by adjusting values prior to 1993 to force agreement with the global mean SSM/I *WV*
197 anomalies over the 1988-1992 period. The influence of water vapour and wind speed changes on *LH*
198 variability (downward defined as positive) are estimated for ERAINT, SSM/I and AMIP5 in Fig. 2.
199 For ERAINT (Fig. 2a-e). The generally positive global net downward *LH* trend in Fig. 2a is due to
200 the increasing *WV* (Fig. 3a) which decreases the surface evaporation, but the effect on the *LH* trend
201 over the *TEP* region is weak. The estimated influence of changes in *U* on surface evaporation is
202 substantial (Fig. 2b). The strong negative trend in downward *LH* over the central and eastern Pacific
203 is driven by the wind speed variability. After combining *U* and *WV*, the trend pattern of *LH* is similar
204 to that using *U* alone (Fig. 2c). When all four actual fields of ERAINT are used, the trend pattern is
205 still dominated by that using the wind speed alone (Fig. 2d) and the *LH* trend of $-0.20 \text{ W/m}^2/\text{yr}$ over
206 *TEP* is still significant (the corresponding global trend of $-0.02 \text{ W/m}^2/\text{yr}$ is small and insignificant),
207 indicating that the wind speed is the driver of negative *LH* trend over *TEP* in ERAINT. Compared
208 with the *LH* trend from direct model output (Fig. 2e), it can be seen that the model generated *LH*
209 trend has more extensive negative trend areas over the whole tropical region, and the *LH* trend over
210 *TEP* is also stronger ($-0.51 \text{ W/m}^2/\text{yr}$, see Fig. 1g). After removing the global *LH* trend, the
211 corresponding *LH* trend of $-0.39 \text{ W/m}^2/\text{yr}$ over *TEP* area is roughly consistent with $-0.18 \text{ W/m}^2/\text{yr}$
212 from the bulk formula, and their correlation coefficient is 0.81 over 1988-2008 (Fig. S3a).

213

214 To check the effect of the data type used in this study on the *LH* estimation, the results from both
215 the daily and monthly data, from the analysis and forecast fields of *SST*, *MSLP*, *WV* and *U*, and from

216 the estimated and model output specific humidities were all tested. The estimated *LH* trends over the
217 *TEP* area from 1988-2008 are -0.23, -0.22 and -0.20 W/m²/yr using the daily forecast, monthly
218 forecast and monthly analysis fields of ERAINT, respectively. Since there is no direct specific
219 humidity output available for us from ERAINT, the JRA55 data are used for the sensitivity test. The
220 estimated *LH* trends are -0.35 and -0.46 W/m²/yr using the estimated specific humidity from *WV* and
221 *SST* and the reanalysis specific humidity, respectively. Therefore the impact of these factors on
222 the *LH* trend over *TEP* area is small, so it is assumed that the discrepancies in spatial structure and
223 values between *LH* estimates from bulk formula and direct model output are mainly due to different
224 bulk formula used in the *LH* calculation. The bulk formula of *Singh et al.* [2005] is applied to the
225 monthly data in this study.

226 Since only *WV* and *U* are available from SSM/I data, the climatologies of four fields from
227 ERAINT are used at first, then the corresponding climatologies are replaced by SSM/I *WV* (Fig. 2f)
228 and SSM/I *U* (Fig. 2g), respectively. The spatial pattern of the SSM/I *WV* effect on *LH* trend is
229 similar to that of ERAINT *WV*. The SSM/I wind speed variability also generates negative downward
230 *LH* trend over *TEP* region, but it is relatively weak compared with that from ERAINT wind speed
231 (Figs. 2b and g). When combining SSM/I *WV* and *U* together, the negative trend over *TEP* area is
232 greatly reduced (Fig. 2h), and it is further smoothed out after the actual fields of *WV* and *U* from
233 SSM/I and *SST* and *MSLP* from ERAINT are used. This indicates that the SSM/I wind speed
234 variability is not large enough to produce the strong negative *LH* trend and this will be further
235 investigated in next section.

236 For the AMIP5 data, the above method is applied to each member and the trends are interpolated
237 into a common grid of 3°x3°, the ensemble mean results are shown in Figs. 2j-m. The spatial pattern
238 of the mean effect of *WV* on *LH* trend (Fig. 2j) is similar to those in Figs. 2a and f, implying similar
239 *WV* trend in three datasets [Allan, 2017]. The wind speed effect is strong in the central Pacific, but
240 weak over *TEP* area where the *LH* trend is overall positive (reduced evaporative flux). The

241 combined WV and U effect enhances the positive trend over TEP region, although the spatial
242 patterns over other regions are similar between these three datasets. After all four fields are used
243 (Fig. 2m), the trend over TEP is very weak (~ -0.02 W/m²/yr) and insignificant (Fig. S3b). The mean
244 LH trend from 15 AMIP5 model simulation ensemble mean is in Fig. 2n, which shows similar but
245 stronger spatial pattern compared to that from bulk formula (Fig. 2m) (spatial correlation $r = 0.61$),
246 particularly the LH trend of 0.11 W/m²/yr over TEP area (Fig. 1h) is stronger, but still insignificant
247 (Fig. S3b). This implies that the application of the bulk formula to the monthly data may smooth the
248 LH calculation, even though the global spatial patterns are still consistent (Figs. 2m and n).
249 Therefore, according to the sensitivity test using bulk formula and direct model output, it is clear that
250 the bulk formula used in this study can reasonably capture aspects of the main features of the
251 corresponding data. Furthermore, these sensitivity tests highlight discrepancies in LH trends between
252 datasets over TEP area and the overall sign of the LH trend depends primarily on the wind speed
253 variability.

254

255 **3.3 Evaluation of water vapor and wind speed trends**

256 To understand the influence of WV and U variability on LH and surface heat flux trend patterns,
257 the trends of WV and U from ERAINT, SSM/I and the AMIP5 ensemble mean over 1988-2008 are
258 investigated (Fig. 3). For WV trends (Figs. 3a-c), the spatial patterns from the three datasets are
259 similar; the trend pattern from ERAINT WV is in close agreement with SSM/I which is unsurprising
260 since this is assimilated by ERAINT over the ice-free oceans. Both JRA55 and MERRA2 show
261 strong positive trends in the central and eastern tropical Pacific (Figs. S4a-b). The similarity of
262 the WV trend across datasets can also be clearly seen from the area mean anomaly time series over
263 TEP (Fig. 3g and Fig. S4e). The WV trends from the AMIP5 ensemble mean (Fig. 3c) and fifteen
264 members (Fig. S5) are also similar. The LH trend spatial pattern in Figs. 2a,f,j and the WV trend

265 spatial pattern in Figs. 3a-c are similar, confirming that the higher *WV* in the atmosphere column will
266 suppress local evaporation.

267 The wind speed trends contrast across datasets. Both ERAINT (Fig. 3d) and JRA55 (Fig. S4c)
268 show strong positive wind speed trends over the central and eastern Pacific, but positive trends from
269 both SSM/I and MERRA2 are much weaker (Fig. 3e and Fig. S4d). This can also be clearly seen
270 from the area mean wind speed anomaly time series over *TEP* as shown in Fig. 3h and Fig. S4f
271 (good agreement between 1995 and 2008 is due to the selection of the reference period of 2001-
272 2008). The trends over 1988-2008 are both 0.26 m/s/decade for ERAINT and JRA55, larger than
273 those from SSM/I (0.10 m/s/decade, Fig. 3e) and the AMIP5 ensemble mean (0.07 m/s/decade, Fig.
274 3f). Although the trends are different, variability is similar (Fig. 3h and Fig. S4f). All AMIP5
275 members show strong wind speed trends in the central Pacific, but weak trends over *TEP* (Fig. S6).

276 In order to see if the *MSLP* drives the wind changes, the *MSLP* trend over 1988-2008 and the
277 multiannual mean were compared (Fig. S7). The similarity of the trend structure in ERAINT (Fig.
278 S7a) and JRA55 (Fig. S7b) in the meridional direction indicates similar gradient changes of *MSLP*
279 between subtropics and equator, which may explain the agreement of wind speed trend structure
280 between them. The relatively weak trend of the subtropical high south of the *TEP* in MERRA2 (Fig.
281 S7c) and AMIP5 (Fig. S7d) indicates weak gradient changes of *MSLP* between the south subtropics
282 and equator, which may explain the weak wind speed trend over *TEP* area. Therefore, although the
283 *MSLP* change over *TEP* area has very small direct effect on the *LH* trend estimation, their spatial
284 structure difference can affect the gradient and further change the wind speed. In addition, *Boisséson*
285 *et al.* [2014] found good agreement for zonal wind speed trends over the tropical Pacific between
286 ERAINT and observations. However they noted that the discontinuities between different satellite
287 products are not taken into account, such as the big jumps between ERS2 (European Remote Sensing
288 satellite) and QSCAT (Quick Scatterometer) near 2000 in their Fig. 2a and between ERS2 and

289 ENVISAT satellite near 2003 in their Fig. 2b. Different conclusions may be obtained if these
290 discontinuities are considered.

291

292 **3.4 Comparison with buoy observations**

293 The large discrepancies in wind speed changes over *TEP* cast doubt on the reliability of the wind
294 speed in these datasets. To further check the wind speed quality, data from TAO moored buoy array
295 (220-255°E, 9°N-8°S) are used in this study for comparison [*TAO Project Office, 2000*]. There are 27
296 buoys working in this area; they are all calibrated before deployment and there is no post-deployment
297 calibration involved. Data quality control information can be found at
298 http://tao.ndbc.noaa.gov/proj_overview/qc_ndbc.shtml. The locations of the buoys are plotted in Fig.
299 4a (colored dots represents the wind speed trend from the buoy), which is an enlargement of Fig. 3d
300 showing the ERAINT wind speed trend. From January 1990 to December 2015, there are 312
301 months; the minimum coverage period from start month to end month over all stations is 202
302 months at station 8N110W (Fig. S8a), so all buoy records span at least 65% of the record length.
303 However, there are considerable gaps in the buoy timeseries: the minimum fraction of the data
304 coverage over 1990-2015 is about 30% at station 5N125W (Fig. S8b) and the mean fraction is 50%.
305 At each station, the anomaly is calculated by removing the monthly mean (over 2001-2008) which is
306 calculated if the total number of months is ≥ 2 . The wind speed anomaly time series is plotted in Fig.
307 S9, but the actual number of valid buoy data points is not well reflected due to the smoothing of six
308 month running mean. The wind speed trends from individual buoy records (Table S1) are generally
309 insignificant: only 9 out of 27 display significant trends and 8 of these are positive (see also Fig. S9)
310 while the composite trend of -0.05 m/s/decade is small and insignificant. 21 out of 27 wind speed
311 trends calculated from ERAINT grid points nearest to the corresponding buoy stations (bottom right
312 matrix of Table S1) are positive and significant, and the composite trend of 0.28 m/s/decade is also
313 significant. When the ERAINT grid box time series are sampled to mimic the intermittent buoy time

314 series (bottom middle matrix of Table S1), 16 out of 27 of the trends remain positive and significant
315 and the composite trend of 0.25 m/s/decade is significant. Therefore, although intermittent data
316 coverage reduces the significance of trends, there are more robust positive trends in the ERA-Interim
317 data when sampled to mimic the buoy spatial and temporal coverage.

318 Mean wind speed variability in the *TEP* for 1990-2008 is displayed in Fig. 4b for ERAINT using a
319 variety of spatial and temporal sampling strategies and the composite of the buoy measurements. The
320 fraction of valid buoy data in each month increases steadily from about 1990 to 2000 and then
321 becomes stable afterwards while there is a drop between 2011 and 2015 (Fig. S8c). Variability in
322 mean ERAINT wind speed over the *TEP* (Fig. 4b, thick red line) is similar to when only grid boxes
323 corresponding to the buoy locations are sampled (cyan line). This indicates that the area mean from
324 the buoy spatial coverage is representative of the wider, completely sampled region; trends over the
325 1990-2015 period are significant (based on the Mann-Kendall test at significance level of 0.05) and
326 positive for both although is larger for the *TEP* region (0.34 m/s/decade) than for the buoy grid
327 points (0.28 m/s/decade). The composite wind speed time series from buoys (Fig. 4b, thick black
328 line) displays an insignificant negative trend of -0.05 m/s/decade over 1990-2008. Sampling
329 ERAINT to also match the temporal coverage of the buoys (magenta line) alters the timeseries
330 substantially demonstrating the substantial effect of incomplete observational coverage. Agreement
331 between ERAINT buoy spatial and temporal sampling (magenta line) and the buoy time series
332 variability is markedly improved ($r = 0.92$), indicating successful assimilation of the observational
333 variability by ERAINT. However, the ERAINT composite (magenta line) trend remains positive
334 (0.25 m/s/decade) and substantially larger than the corresponding trend from the buoy data. The
335 corresponding plot for *LH*, similar to Fig. 4b, is shown in Fig. S8d for reference.

336 The ERAINT minus buoy wind speed difference using consistent spatiotemporal sampling (Fig.
337 4c) depicts an increasing trend (0.14 m/s/decade over 1990-2015) which contributes about 50% to
338 the overall trend of ERAINT wind speed over *TEP*. Thus, the discrepancy between the buoy and

339 ERAINT wind speed trends cannot easily be explained by the variable buoy coverage. It is not
340 currently clear how the assimilation of data from an evolving observing system simply explains this
341 discrepancy and further investigation is merited. The remaining difference is apparently associated
342 with the fact the influence of the assimilation declines rapidly with distance from the buoy as pointed
343 out by *Josey et al.* [2014]. Based on the comparison and analysis, the area mean from the limited
344 buoy spatial coverage (cyan line in Fig. 4b) is representative of that over the wider, completely
345 sampled *TEP* area (red line in Fig. 4b), and the intermittent buoy wind speed variability is well
346 assimilated into the ERA-Interim model. However, increases in the ERAINT minus buoy wind
347 speed, when consistently sampled in space and time, indicate that increases in wind speed and
348 therefore also surface latent heat flux are unrealistic and so the large decreases in net downward
349 energy flux into the tropical eastern Pacific are questionable.

350

351 **4. Conclusions**

352 Cooling of the surface ocean over the tropical eastern Pacific influences the global mean rate of
353 surface temperature change [*Kosaka and Xie, 2013; Trenberth and Fasullo, 2013; England et al.,*
354 *2015*]. In order to understand the mechanism of the cooling, numerous studies have been conducted
355 [*Meehl et al., 2011; Hansen et al., 2011; Guemas et al., 2013; Katsman and van Oldenborgh, 2011;*
356 *Solomon et al., 2010, 2011; Kaufmann et al., 2011; Norris and Evan, 2015; Brown et al. 2014; Zhou*
357 *et al., 2016*]. Motivated by a discrepancy between observations-based estimates of surface heat flux
358 changes and simulations from atmosphere-only models over the *TEP* [*Liu et al. 2015*], an
359 investigation of the causes of the surface energy flux is conducted using data from three atmospheric
360 reanalyses, fifteen AMIP5 model simulations and the DEEPC observations-based reconstruction. It is
361 found that the net downward surface flux change over *TEP* is dominated by the *LH* variability and
362 the trend is significantly negative in ERAINT, JRA55 and DEEPC data. The negative trend
363 over *TEP* from DEEPC is not as strong as that from ERAINT (Figs. 1f and g) due to the contrasting

364 methodologies. In contrast, the F_s and LH trends in AMIP5 ensemble mean show positive trend over
365 TEP region, and the spatial pattern is closely related to the SST pattern, indicating that SST changes
366 are driving heat flux changes in the AMIP5 model simulations. Since the atmosphere simulations do
367 not permit a coupled response to the surface fluxes, it is possible that they are missing an important
368 mechanism yet the negative trends depicted by the reanalysis-based estimates appear unrealistically
369 large.

370 To investigate the realism and cause of the implied changes in surface heat flux, sensitivity tests
371 using turbulent heat flux bulk formula are applied. These indicate that the LH changes depicted by
372 ERAINT are dominated by wind speed changes, which show increasing trends over the eastern
373 Pacific. This wind speed trend is very weak in SSM/I satellite observations and is absent in AMIP5
374 ensemble mean simulations. After further comparison with buoy observations, it is found that few
375 buoy stations show significant positive wind speed trends, although the corresponding composite
376 trends from ERAINT grid points nearest to the stations are significantly positive. The variable spatial
377 coverage of the buoy wind speed is assimilated by ERA-Interim and the buoy coverage is shown to
378 reasonably represent the TEP area mean wind speed (cyan line in Fig. 4b). However, an increase in
379 ERAINT minus buoy wind speed, when consistently sampled in space and time, suggest that the
380 increases in wind speed depicted by ERAINT are overestimated. This further implies that increased
381 evaporative fluxes and reduced downward heat flux trends depicted by ERAINT and other datasets
382 may be unrealistic. The discrepancies between different datasets cast questions on the reliability of
383 the reanalysed surface fluxes over the tropical eastern Pacific area. In AMIP5 simulations, models
384 are forced by SST , so the SST decrease over TEP suppresses the evaporation and reduce the upward
385 LH flux, enhancing the downward net surface flux. In the atmospheric reanalysis, such as the
386 ERAINT the dominant contribution of strong wind speed trend to the LH flux changes is evident.
387 The strong ERAINT LH trend is unrealistic considering the observed temperature changes over TEP
388 region (based upon energy budget arguments) and comparison with buoy data when accounting for

389 sampling. This will indirectly affect the budget-based DEEPC product since erroneous wind speeds
390 will influence the energy transports used in the calculation of surface fluxes; the precise influence is
391 uncertain but has implications for budget-based indirect estimates of surface energy fluxes [*Liu et al.*
392 2017; *Trenberth et al.* 1995; *Chiodo and Haimberger*, 2010; *Mayer and Haimberger*, 2012;
393 *Trenberth and Fasullo*, 2017]. *Josey et al.* [2014] found that assimilation of TAO mooring
394 contributed to unrealistic near surface humidity and wind speed anomalies in ERAINT. The impact
395 of these unrealistic anomalies on the latent heat flux in the tropical Pacific may play a role in the
396 unrealistic *LH* trend. However, these results do not appear to contradict the mechanisms invoked to
397 explain *TEP* cooling discussed by *England et al.* [2014] since this key region of wind enhancement
398 centres on the central pacific where satellite data and simulations broadly agree on recent changes.
399 Nevertheless, the *TEP* is a key region in determining global climate variability and time-varying
400 climate sensitivity [*Ceppi and Gregory*, 2017; *Andrews and Webb*, 2017] so understanding the role
401 of surface fluxes in this region is crucial. While AMIP5 simulations are temporally homogeneous,
402 they do not represent the key atmospheric feedbacks on ocean temperature so additional in-depth
403 investigation is necessary to elucidate the mechanisms of decadal variability in ocean temperature,
404 including using data from the ocean reanalysis and ECMWF ERA5 for further comparisons and
405 coupled reanalysis for feedback mechanism studies.

406

407

408 **Acknowledgements**

409 This work was supported by the Natural Environment Research Council (NERC) DEEP-C grant
410 NE/K005480/1 and SMURPHS grant NE/N006054/1, the National Centre for Atmospheric Science,
411 and the National Centre for Earth Observation. We acknowledge the ECMWF for providing ERA-
412 Interim data. We also acknowledge the teams making the JRA55, MERRA2, AMIP5, SSM/I,
413 CERES and TAO data available. DEEPC data are available at <http://dx.doi.org/10.17864/1947.111>.
414 We thank two anonymous reviewers for reviewing this paper and providing constructive comments
415 and suggestions.

416

417

418

419 **References**

- 420 Allan, R. P., 2017: Decadal climate variability and the global energy balance, *CLIVARExchanges*,
421 No. 72, doi: 10.22498/pages.25.1.20
- 422 Allan, R. P., C. Liu, N. G. Loeb, M. D. Palmer, M. Roberts, D. Smith, and P.-L. Vidale, 2014,
423 Changes in global net radiative imbalance 1985-2012, *Geophys. Res. Lett.*, 41,
424 doi:10.1002/2014GL060962.
- 425 Andrews, T., and M. Webb, 2017: The dependence of global cloud and lapse-rate feedbacks on the
426 spatial structure of tropical Pacific warming. *J. Climate*. doi:10.1175/JCLI-D-17-0087.1, in press.
- 427 Arora, V. K., J. F. Scinocca, G. J. Boer, J. R. Christian, K. L. Denman, G. M. Flato, V. V. Kharin,
428 W. G. Lee, and W. J. Merryfield, 2011: Carbon emission limits required to satisfy future
429 representative concentration pathways of greenhouse gases, *Geophys. Res. Lett.*, 38, L05805,
430 doi:10.1029/2010GL046270.
- 431 Balmaseda, M. A., K. E. Trenberth, and E. Källén, 2013: Distinctive climate signals in reanalysis of
432 global ocean heat content. *Geophys. Res. Lett.*, 40, 1754 - 1759.
- 433 Bentamy, A., K. B. Katsaros, A. M. Mestas-Nuñez, W. M. Drennan, B. E. Forde, and H. Roquet,
434 2003: Satellite estimates of SEPTEMBER 2005 S I N G H E T A L . 2709 wind speed and latent heat
435 flux over the global oceans, *J. Climate*, 16, 637–655.
- 436 Berrisford, P., P. Kållberg, S. Kobayashi, D. Dee, S. Uppala, A. J. Simmons, P. Poli, and H. Sato,
437 2011: Atmospheric conservation properties in ERA-Interim, *Q. J. R. Meteorol. Soc.* 137: 1381–1399,
438 July 2011 B.
- 439 Bi, D., et al., 2013: The ACCESS coupled model: description, control climate and evaluation, *Aust.*
440 *Meteorol. Oceanogr. J.*, 63, 41–64.
- 441 Boisséson, E., M. A. Balmaseda, S. Abdalla, E. Källén, and P. Janssen, 2014: How robust is the
442 recent strengthening of the Tropical Pacific trade winds? *Geophys. Res. Lett.*, 41, 4398-4405.

443 Brown, P. T., W. Li, L. Li, and Y. Ming, 2014: Top-of-atmosphere radiative contribution to unforced
444 decadal global temperature variability in climate models, *Geophys. Res. Lett.*, 41, 5175–5183,
445 doi:10.1002/2014GL060625.

446 Ceppi P., and J. M. Gregory, 2017: Relationship of tropospheric stability to climate sensitivity and
447 Earth’s observed radiation budget, *PNAS*, XXX

448 Cheng, L., K. E. Trenberth, J. Fasullo, T. Boyer, J. Abraham, and J. Zhu, 2017: Improved estimates
449 of ocean heat content from 1960 to 2015, *Science Advances*, 3, e1601545
450 doi: 10.1126/sciadv.1601545

451 Chiodo, G., and L. Haimberger, 2010: Interannual changes in mass consistent energy budgets from
452 ERA-Interim and satellite data, *J. Geophys. Res.*, 115, D02112, doi:10.1029/2009JD012049.

453 Collins, W. J., et al., 2011: Development and evaluation of an Earth-system model—HadGEM2,
454 *Geosci. Model Dev. Discuss.*, 4, 997–1062, doi:10.5194/gmdd-4-997-2011.

455 Compo, G. P. et al., 2011: The twentieth century reanalysis project. *Q. J. R. Meteorol.*
456 *Soc.* 137(654), 1-28. DOI: 10.1002/qj.776

457 Dee, D. P., et al., 2011: The ERA-Interim reanalysis: Configuration and performance of the data
458 assimilation system, *Q. J. R. Meteorol. Soc.*, 137, 553–597, doi:10.1002/qj.828.

459 Delworth, T. L., et al., 2006: GFDL’s CM2 global coupled climate models. Part I: Formulation and
460 simulation characteristics, *J. Clim.*, 19, 643–674, doi:10.1175/JCLI3629.1.

461 Dufresne, J. L., et al., 2013: Climate change projections using the IPSL-CM5 Earth System Model:
462 From CMIP3 to CMIP5, *Clim. Dyn.*, 40, 2123–2165, doi:10.1007/s00382-012-1636-1.

463 Easterling, D. R., and M.F. Wehner, 2009: Is the climate warming or cooling? *Geophys. Res. Lett.* 36,
464 L08706, doi:10.1029/2009GL037810.

465 England, M. H., S. McGregor, P. Spence, G. A. Meehl, A. Timmermann, W. Cai, A. S. Gupta, M. J.
466 McPhaden, A. Purich, and A. Santoso, 2014: Recent intensification of wind-driven circulation in the
467 Pacific and the ongoing warming hiatus, *Nat. Clim. Change*, 4, 222–227, doi:10.1038/nclimate2106.

468 Gelaro, R., and Coauthors, 2017: The Modern-Era Retrospective Analysis for Research and
469 Applications, version 2 (MERRA-2). *J. Climate*, 30, 5419-5454, [https://doi.org/10.1175/JCLI-D-16-](https://doi.org/10.1175/JCLI-D-16-0758.1)
470 0758.1.

471 Gent, P. R., et.al., 2011: The Community Climate System Model version 4, *J. Clim.*, 24, 4973–4991,
472 doi:10.1175/2011JCLI4083.1.

473 Guemas, V., F. J. Doblas-Reyes, I. Andreu-Burillo, and M. Asif, 2013: Retrospective prediction of
474 the global warming slowdown in the past decade. *Nature Clim. Change* **3**, 649_653.

475 Hansen, J., M. Sato, P. Kharecha, and K. von Schuckmann, 2011: Earth’s energy imbalance and
476 implications, *Atmos. Chem. Phys.*, 11, 13,421–13,449, doi:10.5194/acp-11-13421-2011.

477 Hipel, K.W., and A. I. McLeod, 1994: *Time Series Modelling of Water Resources and*
478 *Environmental Systems*, Amsterdam: Elsevier. ISBN: 0-444-89270-2

479 Huber, M., and R. Knutti, 2014: Natural variability, radiative forcing and climate response in the
480 recent hiatus reconciled, *Nature GeoScience*, 7, doi: 10.1038/NGEO2228.

481 Josey, S. A., L. Yu, S. Gulev, X. Jin, N. Tilinina, B. Barnier, and L. Brodeau, 2014: Unexpected
482 impacts of the Tropical Pacific array on reanalysis surface meteorology and heat fluxes, *Geophys.*
483 *Res. Lett.*, 41, 6213–6220, doi:10.1002/2014GL061302.

484 Katsman, C. A., and G. J. van Oldenborgh, 2011: Tracing the upper ocean's missing heat. *Geophys.*
485 *Res. Lett.* **38**, L14610.

486 Kaufmann, R. K., H. Kauppib, M. L. Mann, and J. H. Stock, 2011: Reconciling anthropogenic
487 climate change with observed temperature 1998_2008. *Proc. Natl Acad. Sci. USA* **108**, 790_793
488 (2011).

489 Klein, S. A., and D. L. Hartmann, 1993: The seasonal cycle of low stratiform clouds, *J. Clim.*, 6, 1587–
490 1606.

491 Knight, J., J. J. Kennedy, C. Folland, G. Harris, G. S. Jones, M. Palmer, D. Parker, A. Scaife, and P.
492 Stott, 2009: Do global temperature trends over the last decade falsify climate predictions? [in "State
493 of the Climate in 2008"]. *Bull. Amer. Meteor. Soc.*, *90*, S22-S23.

494 Kobayashi, S., Y. Ota, Y. Harada, A. Ebita, M. Moriya, H. Onoda, K. Onogi, H. Kamahori, C.
495 Kobayashi, H. Endo, K. Miyaoka, and K. Takahashi, 2015: The JRA-55 Reanalysis: General
496 specifications and basic characteristics. *J. Meteor. Soc. Japan*, **93**, 5-48, doi:10.2151/jmsj.2015-001.

497 Kosaka, Y., and S. P. Xie, 2013 Recent global-warming hiatus tied to equatorial Pacific surface
498 cooling, *Nature*, *501*, 403–407, doi:10.1038/nature12534.

499 Li, L., et al., 2013: The flexible global ocean–atmosphere–land system model, Grid-point version 2:
500 FGOALS-s2, *Adv. Atmos. Sci.*, *30*, 543–560, doi:10.1007/s00376-012-2140-6.

501 Liu, C., R. P. Allan, P. Berrisford, M. Mayer, P. Hyder, N. Loeb, D. Smith, P.-L. Vidale, and J. M.
502 Edwards, 2015: Combining satellite observations and reanalysis energy transports to estimate global
503 net surface energy fluxes 1985-2012. *J. Geophys. Res., Atmospheres*. ISSN 2169-8996 doi:
504 10.1002/2015JD023264.

505 Liu, C., R. P. Allan, M. Mayer, P. Hyder, N. G. Loeb, C. D. Roberts, M. sJ. M. Edwards, and P.-L.
506 Vidale, 2017: Evaluation of satellite and reanalysis-based global net surface energy flux and
507 uncertainty estimates. *J. Geophys. Res., Atmospheres*, *122* (12). pp. 6250-6272. ISSN 2169-8996
508 doi: 10.1002/2017JD026616

509 Loeb, N. G., J. M. Lyman, G. C. Johnson, R. P. Allan, D. R. Doelling, T. Wong, B. J. Soden, and G.
510 L. Stephens, 2012: Observed changes in top-of-atmosphere radiation and upper-ocean heating
511 consistent within uncertainty, *Nature Geoscience*, *5*, 110-113.

512 Lucchesi, R., 2012: File Specification for MERRA Products. GMAO Office Note No. 1 (Version
513 2.3), 82 pp, available from http://gmao.gsfc.nasa.gov/pubs/office_notes.

514 Mayer, M., and L. Haimberger, 2012: Poleward Atmospheric Energy Transports and Their
515 Variability as Evaluated from ECMWF Reanalysis Data, *J. Climate*, 25, 734–752, doi:
516 <http://dx.doi.org/10.1175/JCLI-D-11-00202.1>.

517 Meehl, G. A., J. M. Arblaster, J. Y. Fasullo, A. Hu, and K. E. Trenberth, 2011: Model-based
518 evidence of deep-ocean heat uptake during surface-temperature hiatus periods. *Nature Clim. Change*
519 **1**, 360_364.

520 Meehl, G. A., H. Teng, and J. M. Arblaster, 2014: Climate model simulations of the observed early-
521 2000s hiatus of global warming, *Nat. Clim. Change*, 4, 898–902, doi:10.1038/NCLIMATE2357.

522 Norris, J. R. and A. T. Evan, 2015: Empirical removal of artifacts from the ISCCP and PATMOS-x
523 satellite cloud records. *J. Atmos. Ocean. Technol.* **32**, 691-702.

524 Raddatz, T. J., C. H. Reick, W. Knorr, J. Kattge, E. Roeckner, R. Schnur, K.-G. Schnitzler, P.
525 Wetzel, and J. Jungclaus, 2007: Will the tropical land biosphere dominate the climate-carbon cycle
526 feedback during the twenty first century?, *Clim. Dyn.*, 29, 565–574, doi:10.1007/
527 s00382-007-0247-8.

528 Roberts, C. D., M. D. Palmer, R. P. Allan, D. G. Desbruyeres, P. Hyder, C. Liu, and D. Smith, 2017:
529 Surface flux and ocean heat transport convergence contributions to seasonal and interannual
530 variations of ocean heat content, *J. Geophys. Res. Oceans*, 122, doi:10.1002/2016JC012278.

531 Schmidt, G. A., et al., 2014: Configuration and assessment of the GISS ModelE2 contributions to the
532 CMIP5 archive, *J. Adv. Model. Earth Syst.*, 6, 141–184, doi:10.1002/2013MS000265.

533 Scoccimarro, E., S. Gualdi, A. Bellucci, A. Sanna, P. G. Fogli, E. Manzini, M. Vichi, P. Oddo, and
534 A. Navarra, 2011: Effects of tropical cyclones on ocean heat transport in a high resolution coupled
535 general circulation model, *J. Clim.*, 24, 4368–4384.

536 Senior, C.A., et al., 2016: Idealised climate change simulations with a high resolution physical
537 model: HadGEM3-GC2. *J. Adv. Model. Earth Syst.*, doi:10.1002/2015MS000614.

538 Singh, R., P. C. Joshi, and C. M. Kishtawal (2005), A new technique for estimation of surface latent
539 heat fluxes using satellite - based observations, *Mon. Weather Rev.*, 133, 2692–2710,
540 doi:10.1175/MWR2993.1.

541 Solomon, S. et al., 2010: Contributions of stratospheric water vapor to decadal changes in the rate of
542 global warming. *Science* **327**, 1219_1223.

543 TAO Project Office, 2000: Tropical Atmosphere Ocean/Triangle Trans-Ocean Buoy Network.
544 NOAA/PMEL, accessed 1 August 2015. [Available online at [http://www.pmel.noaa.gov/tao/
545 data_deliv/deliv.html.](http://www.pmel.noaa.gov/tao/data_deliv/deliv.html)]

546 Taylor, K. E., R. J. Stouffer, and G. A. Meehl, 2012: An overview of CMIP5 and the experiment
547 design, *Bull. Am. Meteorol. Soc.*, 93, 485–98.

548 Trenberth, K. E., and J. T. Fasullo, 2013: An apparent hiatus in global warming? *Earth's Future*, doi:
549 10.002/2013EF000165.

550 Trenberth, K. E., and J. T. Fasullo, 2017: Atlantic meridional heat transports computed from
551 balancing Earth's energy locally, *Geophys. Res. Lett.*, 44 , 1919 1927, doi:10.1002/2016GL072475.

552 Trenberth, K. E., J. W. Hurrell, and A. Solomon, 1995: Conservation of mass in 3-dimensions in
553 global analyses. *J. Climate*, 8, 692–708.

554 Valdivieso, M., Haines, K., Balmaseda, M., Chang, Y.-S., Drevillon, M., Ferry, N., Fujii, Y., Kohl,
555 A., Storto, A., Toyoda, T., Wang, X., Waters, J., Xue, Y., Yin, Y., Barnier, B., Hernandez, F., Kumar,
556 A., Lee, T., Masina, S. and Peterson, K. A., 2015: An assessment of air-sea heat fluxes from ocean
557 and coupled reanalyses. *Climate Dynamics*. ISSN 0930-7575 doi:10.1007/s00382-015-2843-3.

558 Vila, D., D. R. Ferraro, and H. Semunegus, 2010: Improved global rainfall retrieval using the Special
559 Sensor Microwave Imager (SSM/I), *J. Appl. Meteorol. Climatol.*, 49, 1032–1043,
560 doi:10.1175/2009JAMC2294.1.

561 Voltaire, A., et al., 2012: The CNRM-CM5.1 global climate model: Description and basic
562 evaluation, *Clim. Dyn.*, 40, 2091–2121, doi:10.1007/s00382-011-1259-y.

563 Volodin, E. M., N. A. Dianskii, and A. V. Gusev, 2010: Simulating present-day climate with the
564 INMCM4.0 coupled model of the atmospheric and oceanic general circulations, *Izv. Atmos. Oceanic*
565 *Phys.*, 46, 414–431, doi:10.1134/S000143381004002X.

566 Von Schuckmann, K., and Coauthors, 2016: An imperative to monitor Earth's energy imbalance.
567 *Nat. Clim. Change*, 6, 138-144.

568 Watanabe, M., H. Shiogama, H. Tatebe, M. Hayashi, M. Ishii, and M. Kimoto, 2014: Contribution of
569 natural decadal variability to global warming acceleration and hiatus, *Nature Climate Change*, 4, doi:
570 10.1038/NCLIMATE2355.

571 Watanabe, S., et al., 2011: MIROC-ESM 2010: Model description and basic results of CMIP5-
572 20c3m experiments, *Geosci. Model Dev.*, 4, 845–872, doi:10.5194/gmd-4-845-2011.

573 Wentz, F. J., and R. W. Spencer, 1998: SSM/I rain retrievals within a unified all-weather ocean
574 algorithm, *J. Atmos. Sci.*, 55, 1613–1627, doi:10.1175/1520-
575 0469(1998)055<1613:SIRRWA>2.0.CO;2.

576 Williams, K. D., C. M. Harris, A. Bodas-Salcedo, J. Camp, R. E. Comer, D. Copsey, D. Fereday, T.
577 Graham, R. Hill, T. Hinton, P. Hyder, S. Ineson, G. Masato, S. F. Milton, M. J. Roberts, D. P.
578 Rowell, C. Sanchez, A. Shelly, B. Sinha, D. N. Walters, A. West, T. Woollings, and P. K. Xavier,
579 2015: The Met Office Global Coupled model 2.0 (GC2) configuration, *Geosci. Model Dev.*, 8, 1509-
580 1524, doi:10.5194/gmd-8-1509-2015.

581 Yukimoto, S., et al., 2012: A new global climate model of meteorological research institute: MRI-
582 CGCM3—Model description and basic performance, *J. Meteorol. Soc. Jpn.*, 90, 23–64.

583 Zhang, Z. S., K. Nisancioglu, M. Bentsen, J. Tjiputra, I. Bethke, Q. Yan, B. Risebrobakken, C.
584 Andersson, and E. Jansen, 2012: Pre-industrial and mid-Pliocene simulations with NorESM-L,
585 *Geosci. Model Dev. Discuss.*, 5, 119–148, doi:10.5194/gmdd-5-119-2012.

586 Zhou, C., M. D. Zelinka and S. A. Klein, 2016: Impact of decadal cloud variations on the Earth's
587 energy budget, *Nature Geosci.*, DOI: 10.1038/NGEO2828.

588

589

590

591

Table 1. Datasets

| Dataset | Period (in this study) | Resolution | References |
|---|-------------------------------------|--|--|
| Reconstruct (DEEPC) Surface net flux: F_s | 1985-2015 | $0.7^\circ \times 0.7^\circ$ | <i>Liu et al.</i> [2015, 2017] |
| CERES | 2001-2016 | $1.0^\circ \times 1.0^\circ$ | <i>Loeb et al.</i> [2012] |
| SSM/I F08 F11 F13 | 1987-2016 | $0.25^\circ \times 0.25^\circ$ | <i>Wentz and Spencer</i> [1998] <i>Vila et al.</i> [2010] |
| Atmospheric reanalyses ERA-Interim (ERAINT) JRA55 MERRA2 | 1985-2015 1985-2014 1985-2016 | $0.7^\circ \times 0.7^\circ$ $0.56^\circ \times 0.56^\circ$ $0.5^\circ \times 0.625^\circ$ | <i>Dee et al.</i> [2011] <i>Kobayashi et al.</i> [2015] <i>Gelaro et al.,</i> [2017] |
| TAO buoy | 1990-2017 | | <i>TAO Project Office,</i> [2000] |
| AMIP5 models | 1985-2008 | | |
| ACCESS1-0 | | $1.25^\circ \times 1.875^\circ$ | <i>Bi et al.</i> [2013] |
| CanAM4 | | $2.79^\circ \times 2.81^\circ$ | <i>Arora et al.</i> [2011] |
| CCSM4 | | $0.94^\circ \times 1.25^\circ$ | <i>Gent et al.</i> [2011] |
| CMCC-CM | | $0.75^\circ \times 0.75^\circ$ | <i>Scoccimarro et al.</i> [2011] |
| CNRM-CM5 | | $1.40^\circ \times 1.41^\circ$ | <i>Voldoire et al.</i> [2012] |
| FGOALS-g2 | | $3.0^\circ \times 2.81^\circ$ | <i>Li et al.</i> [2013] |
| GFDL-CM3 | | $2.0^\circ \times 2.5^\circ$ | <i>Delworth et al.</i> [2006] |
| GISS-E2-R | | $2.0^\circ \times 2.5^\circ$ | <i>Schmidt et al.</i> [2014] |
| HadGEM2-A | | $1.25^\circ \times 1.875^\circ$ | <i>Collins et al.</i> [2011] |
| INM-CM4 | | $1.5^\circ \times 2.0^\circ$ | <i>Volodin et al.</i> [2010] |
| IPSL-CM5A-LR | | $1.89^\circ \times 3.75^\circ$ | <i>Dufresne et al.</i> [2013] |
| MIROC5 | | $1.39^\circ \times 1.41^\circ$ | <i>Watanabe et al.</i> [2011] |
| MPI-ESM-LR | | $1.85^\circ \times 1.875^\circ$ | <i>Raddatz et al.</i> [2007] |
| MRI-CGCM3 | | $1.11^\circ \times 1.13^\circ$ | <i>Yukimoto et al.</i> [2012] |
| NorESM1-M | | $1.89^\circ \times 2.5^\circ$ | <i>Zhang et al.</i> [2012] |

592

593 **Figure captions**

594

595 **Fig. 1.** Left column is the trend of (a) *SST* and (b-d) net surface flux over 1988-2008. Right column
596 is the corresponding area mean anomaly time series over tropical eastern Pacific (marked area: from
597 20°N–20°S and 210°E to the west coast of Central America). Four components of F_s are also plotted
598 in g and h, and the *SW* and *LW* from CERES are plotted in f, together with the turbulent flux derived
599 from the difference between DEEPC net surface flux and CERES radiation fluxes. The reference
600 period is 2001-2008. The datasets are from ERAINT, DEEPC and AMIP5 15 member ensemble. All
601 fluxes are downward positive. All lines are six month running means and some linear trends are also
602 displayed.

603

604 **Fig. 2.** Sensitivity test of *LH* trend using bulk formula over 1988-2008. The climatologies of *SST*,
605 *MSLP*, *WV* and wind speed from ERAINT are used at first, then the corresponding climatologies are
606 replaced by (a) ERAINT *WV*, (b) ERAINT wind speed, (c) ERAINT *WV* and wind speed, (d) all
607 four fields from ERAINT, (f) SSM/I *WV*, (g) SSM/I wind speed, (h) SSM/I *WV* and wind speed and
608 (i) *WV* and wind speed from SSM/I, *SST* and *MSLP* from ERAINT. The *LH* trend from directly
609 ERAINT reanalysis is in (e). The same method is applied to each of 15 AMIP5 models, and the
610 ensemble means are plotted in (j-m). The mean *LH* trend from 15 AMIP5 model simulations is in
611 (n).

612

613 **Fig. 3.** (a-f) Trends of *WV* and wind speed over 1988-2008 from ERAINT, SSM/I and AMIP5
614 ensemble mean. (g-h) Corresponding deseasonalized time series of area mean *WV* and wind speed
615 over *TEP*. The shaded areas of AMIP5 are 15-member ensemble mean (solid black line) ± 1 standard
616 deviation. The reference period is 2001-2008 for anomaly calculation. The wind speed trends over
617 1988-2008 are also displayed in (h).

618 **Fig. 4.** (a) Wind speed trend from ERAINT (enlargement of Fig. 4d). Colored dots indicate 27 TAO
619 buoy locations and wind speed trends. (b) Deseasonalized wind speed anomaly (relative to 2001–
620 2008 period) time series from buoy stations (composite, thick black line), ERAINT area weighted
621 mean over *TEP* (thick red line), ERAINT mean from grid points nearest to buoy stations including
622 all data points (thick cyan line, no area weighting) and the ERAINT mean including data points
623 where the buoy station has the valid data (magenta line, no area weighting). All lines are 12 month
624 running mean. (c) The time series of mean wind speed bias between ERAINT and buoy data using
625 consistent spatiotemporal sampling. The trend of 0.14/m/s/decade over 1990-2015 is also displayed.
626
627

628
629
630
631
632
633
634
635
636
637
638
639
640
641
642
643
644
645
646
647
648
649
650
651
652
653
654
655
656
657
658
659
660
661
662

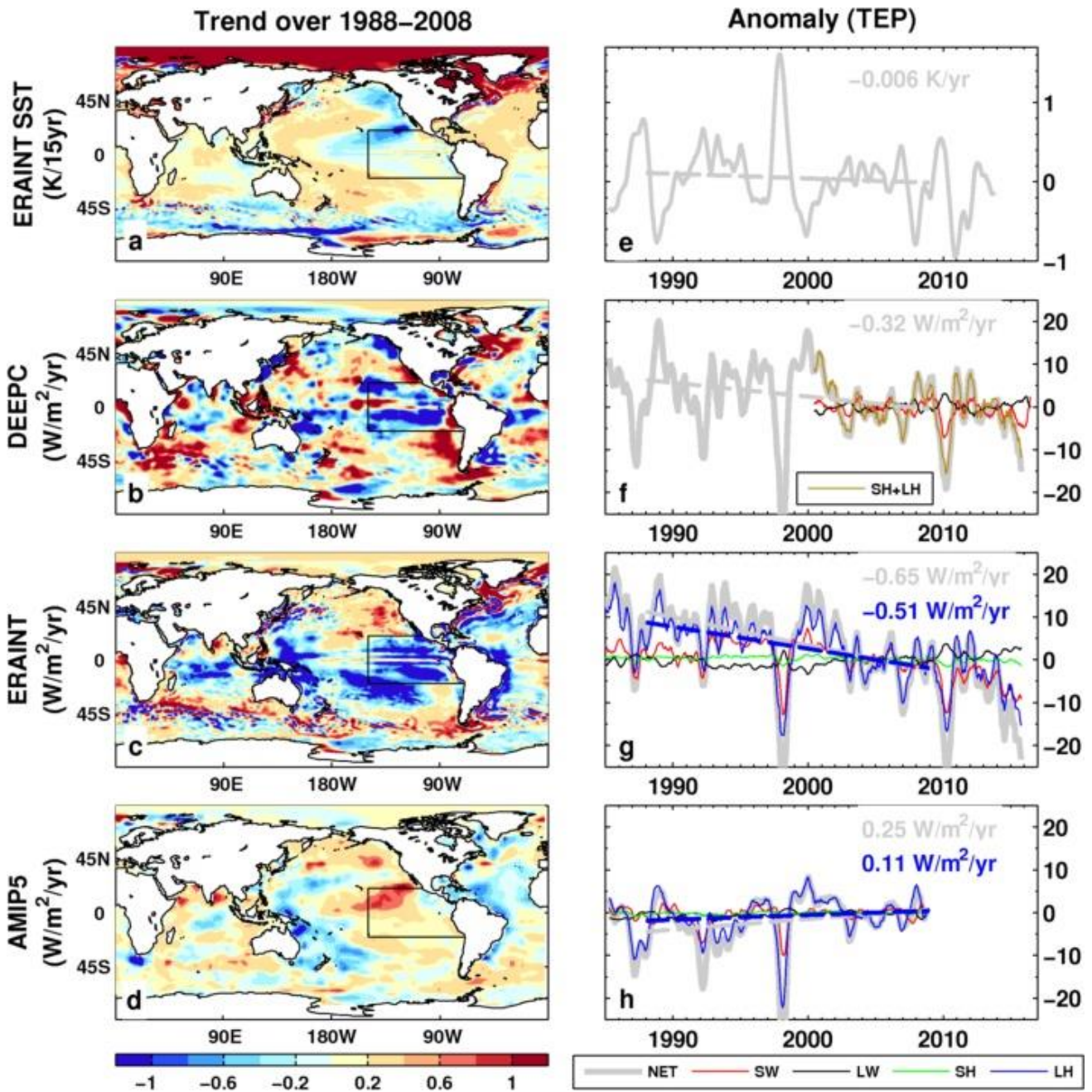
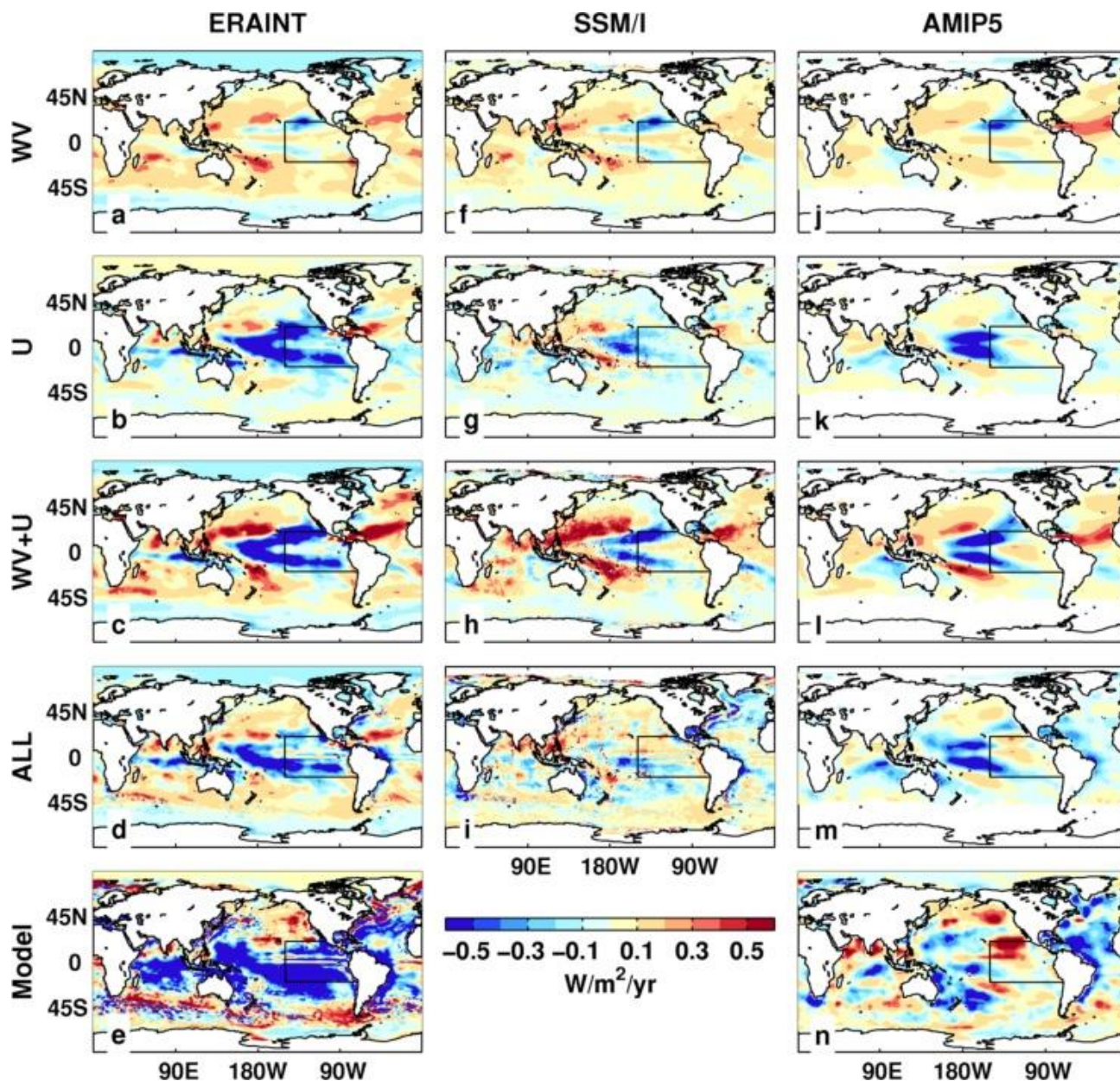


Fig. 1. Left column is the trend of (a) SST and (b-d) net surface flux over 1988-2008. Right column is the corresponding area mean anomaly time series over tropical eastern Pacific (marked area: from 20°N–20°S and 210°E to the west coast of Central America). Four components of F_s are also plotted in g and h, and the SW and LW from CERES are plotted in f, together with the turbulent flux derived from the difference between DEEPC net surface flux and CERES radiation fluxes. The reference period is 2001-2008. The datasets are from ERAINT, DEEPC and AMIP5 15 member ensemble. All fluxes are downward positive. All lines are six month running means and some linear trends are also displayed.

663
664
665
666
667
668
669
670
671
672
673
674
675
676
677
678
679
680
681
682
683
684
685



686
687
688
689
690
691
692
693
694

Fig. 2. Sensitivity test of *LH* trend using bulk formula over 1988-2008. The climatologies of *SST*, *MSLP*, *WV* and wind speed from ERAINT are used at first, then the corresponding climatologies are replaced by (a) ERAINT *WV*, (b) ERAINT wind speed, (c) ERAINT *WV* and wind speed, (d) all four fields from ERAINT, (f) SSM/I *WV*, (g) SSM/I wind speed, (h) SSM/I *WV* and wind speed and (i) *WV* and wind speed from SSM/I, *SST* and *MSLP* from ERAINT. The *LH* trend from directly ERAINT reanalysis is in (e). The same method is applied to each of 15 AMIP5 models, and the ensemble means are plotted in (j-m). The mean *LH* trend from 15 AMIP5 model simulations is in (n).

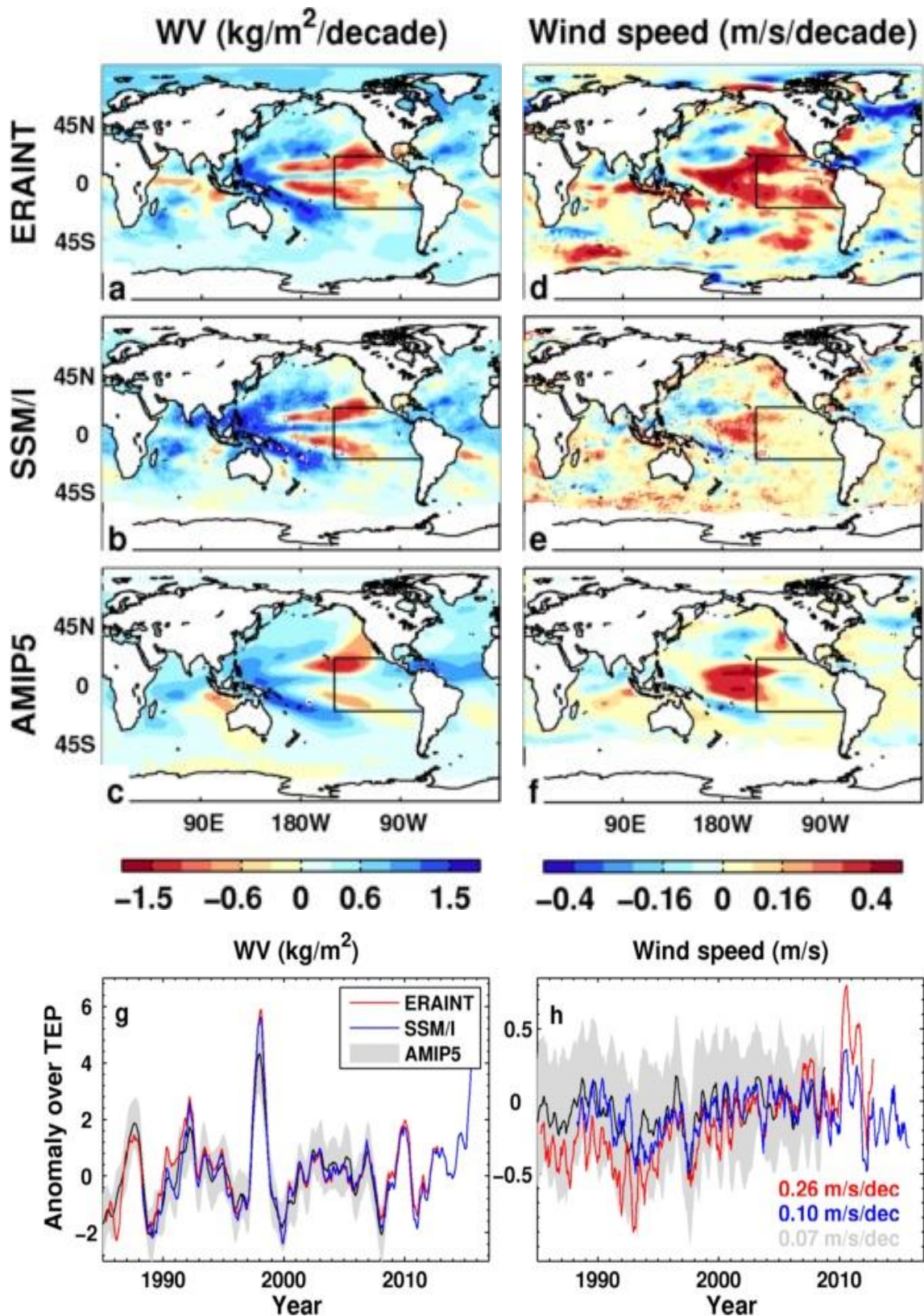


Fig. 3. (a-f) Trends of WV and wind speed over 1988-2008 from ERAINT, SSM/I and AMIP5 ensemble mean. (g-h) Corresponding deseasonalized time series of area mean WV and wind speed over TEP . The shaded areas of AMIP5 are 15-member ensemble mean (solid black line) ± 1 standard deviation. The reference period is 2001-2008 for anomaly calculation. The wind speed trends over 1988-2008 are also displayed in (h).

727
728
729
730
731
732
733
734
735
736
737
738
739
740
741
742
743
744
745
746
747
748
749
750
751
752
753
754
755
756
757
758
759
760

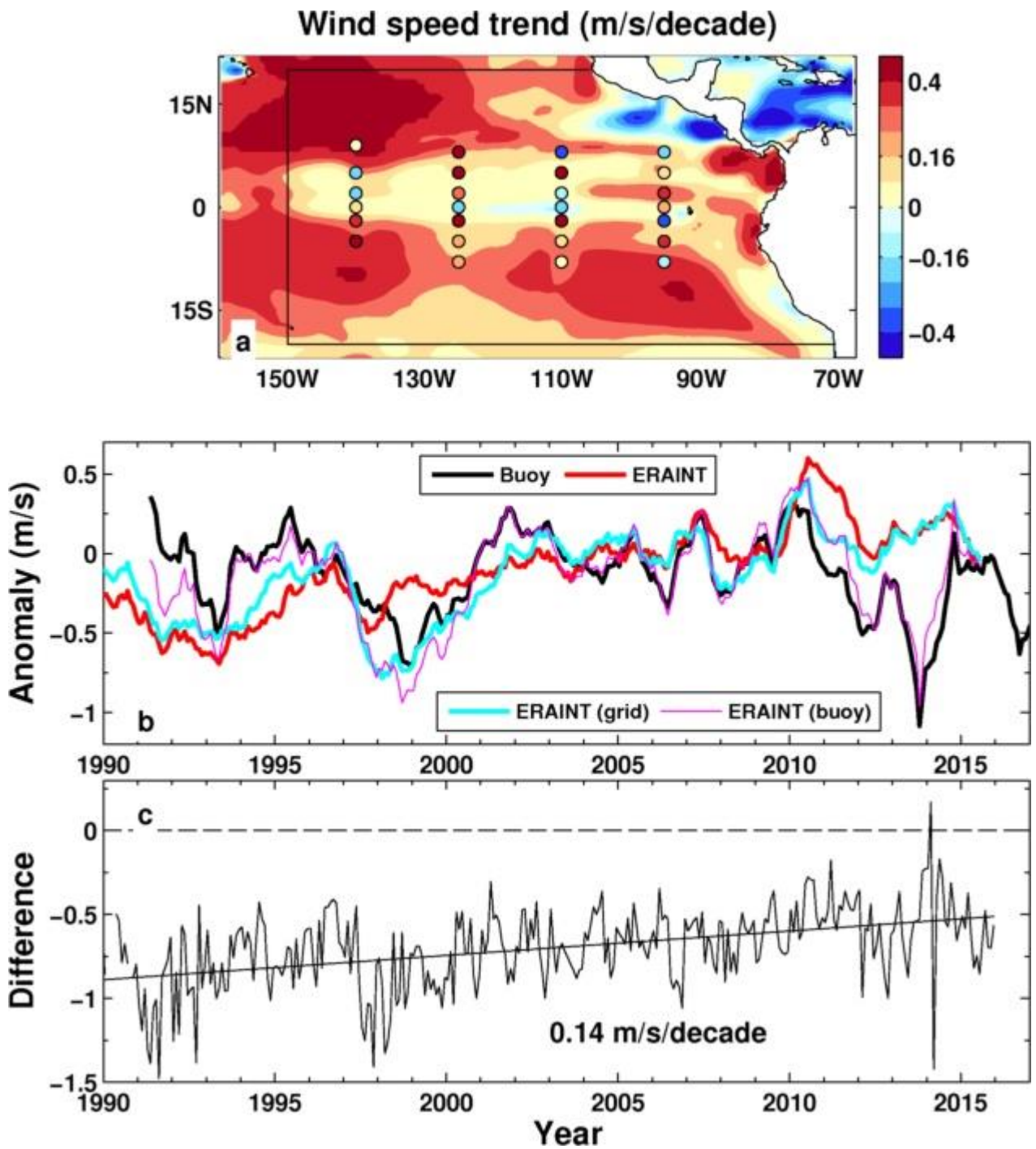


Fig. 4. (a) Wind speed trend from ERAINT (enlargement of Fig. 4d). Colored dots indicate 27 TAO buoy locations and wind speed trends. (b) Deseasonalized wind speed anomaly (relative to 2001–2008 period) time series from buoy stations (composite, thick black line), ERAINT area weighted mean over *TEP* (thick red line), ERAINT mean from grid points nearest to buoy stations including all data points (thick cyan line, no area weighting) and the ERAINT mean including data points where the buoy station has the valid data (magenta line, no area weighting). All lines are 12 month running mean. (c) The time series of mean wind speed bias between ERAINT and buoy data using consistent spatiotemporal sampling. The trend of 0.14/m/s/decade over 1990–2015 is also displayed.